

Hydrophobic and Hydrophilic Solid-Fluid Interaction

JINYUAN LIU, MENGDI WANG, FAN FENG, ANNIE TANG, QIQIN LE, and BO ZHU,
Dartmouth College, USA

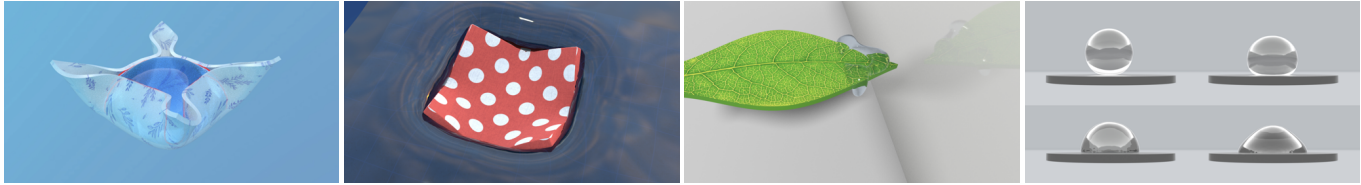


Fig. 1. We simulated several elastocapillary phenomena demonstrating the different types of hydrophobic and hydrophilic interactions between surface tension and deformable objects. (*Far Left*) Capillary origami: spontaneous wrapping of a droplet with an elastic planar solid. (*Middle Left*) A heavy soft object falling into a liquid with strong surface tension. (*Middle Right*) Colliding and bouncing of a droplet on a hydrophobic leaf. (*Far Right*) Contact angles between surface-tension droplets and surfaces with different wettabilities.

We propose a novel solid-fluid coupling method to capture the subtle hydrophobic and hydrophilic interactions between liquid, solid, and air at their multi-phase junctions. The key component of our approach is a Lagrangian model that tackles the coupling, evolution, and equilibrium of dynamic contact lines evolving on the interface between surface-tension fluid and deformable objects. This contact-line model captures an ensemble of small-scale geometric and physical processes, including dynamic water-front tracking, local momentum transfer and force balance, and interfacial tension calculation. On top of this contact-line model, we further developed a mesh-based level set method to evolve the three-phase T-junction on a deformable solid surface. Our dynamic contact-line model, in conjunction with its monolithic coupling system, unifies the simulation of various hydrophobic and hydrophilic solid-fluid-interaction phenomena and enables a broad range of challenging small-scale elastocapillary phenomena that were previously difficult or impractical to solve, such as the elastocapillary origami and self-assembly, dynamic contact angles of drops, capillary adhesion, as well as wetting and splashing on vibrating surfaces.

CCS Concepts: • **Computing methodologies** → **Modeling and simulation**.

Additional Key Words and Phrases: solid-fluid coupling, surface tension, elastocapillarity, contact line

ACM Reference Format:

Jinyuan Liu, Mengdi Wang, Fan Feng, Annie Tang, Qiqin Le, and Bo Zhu. 2022. Hydrophobic and Hydrophilic Solid-Fluid Interaction. *ACM Trans. Graph.* 41, 4, Article 256 (July 2022), 15 pages. <https://doi.org/10.1145/3550454.3555478>

Authors' address: Jinyuan Liu, jinyuan.liu.gr@dartmouth.edu; Mengdi Wang, mengdi.wang.gr@dartmouth.edu; Fan Feng, fan.feng.gr@dartmouth.edu; Annie Tang, Annie.Tang.25@dartmouth.edu; Qiqin Le, leqiqin80@gmail.com; Bo Zhu, bo.zhu@dartmouth.edu, Computer Science Department, Dartmouth College, Hanover, USA, (Qiqin Le was a research intern at Dartmouth College during this work).

Permission to make digital or hard copies of all or part of this work for personal or classroom use is granted without fee provided that copies are not made or distributed for profit or commercial advantage and that copies bear this notice and the full citation on the first page. Copyrights for components of this work owned by others than ACM must be honored. Abstracting with credit is permitted. To copy otherwise, or republish, to post on servers or to redistribute to lists, requires prior specific permission and/or a fee. Request permissions from permissions@acm.org.

© 2022 Association for Computing Machinery.

0730-0301/2022/7-ART256 \$15.00

<https://doi.org/10.1145/3550454.3555478>

1 INTRODUCTION

Hydrophobic and hydrophilic solid-fluid interactions are widely seen in nature. Examples range from raindrops splashing on vibrating foliage and dewdrops sliding on the strands of the spider webs to plant transpiration and aquatic insect locomotion. A number of visually interesting coupling phenomena have been observed in laboratory experiments, such as a compliant sheet deforming under capillary forces [Roman and Bico 2010], a porous solid absorbing liquid [Hao et al. 2015], and a lattice structure intriguing capillary rises [Dudukovic et al. 2021]. Some of these phenomena, such as dewdrops and insect locomotion, are hydrophobic, in which the fluid and solid interfaces tend to repel each other due to the dominant molecular cohesion [Pratt and Chandler 1977]. Some others, like wicking and wetting, are hydrophilic, in which the solid and water interfaces attract each other due to the strong intermolecular adhesion. Some phenomena are in between these two categories, such as raindrop-foliage interactions, exhibiting a spectrum of fluid and solid behaviors that depend on the comparable adhesive and cohesive effects on the dynamic interface.

Small-scale interactions between liquids and solids are dominated by surface stresses that measure the amount of work per unit area needed to stretch a surface elastically. Surface tension on a liquid-air interface, which underpins many visually attractive small-scale flow phenomena, is one specific type of stress. In addition to the liquid-air surface tension, a liquid-solid interface or a solid-air interface also manifests surface stresses between highly compliant solids (e.g., thin membranes and gels) and surface-tension liquid. These coupling phenomena, whose dynamics are dominated by the strong interaction between surface stresses and elasticity, are known as *elastocapillarity* in engineering and physical sciences and have received extensive attention over the past decade.

In theoretical and experimental physics, a vast majority of literature has been devoted to studying the coupling mechanics underpinning elastocapillarity (see [Butt and Kappl 2018; Cao et al. 2014; Liu and Feng 2012] for a comprehensive survey). At the heart of these research efforts lie the study of contact-line dynamics (e.g., see [Fan et al. 2020; Liang et al. 2018]). Geometrically, a contact line is featured by a codimension-two curve on two codimension-one

surfaces in contact. Physically, the force balance on the contact line among multiple phases controls the system's hydrophobicity and hydrophilicity. The interleaving complexities between the dynamic geometry and multi-phase physics rendered the elastocapillary phenomena challenging to model. Existing mathematical and computational models can handle specific capillary phenomena, such as the one-dimensional necking [Lestringant and Audoly 2020], elastocapillary rise [Duprat et al. 2011], and the dynamics of a single straight contact line [Limat 2012]. However, none of these approaches is scalable and generalizable in complex three-dimensional settings to produce visually authentic simulations.

In computer graphics, researchers have studied the static contact angles between liquid drops and rigid boundaries with different wettability and produced realistic animations, ranging from creeping droplets [Wang et al. 2005] and cracking eggs [Yang et al. 2017] to melting candles and tears of wine [Chen et al. 2021]. Despite these impressive successes, the simulation of interactions between surface tension liquid and deformable solids, especially elastocapillarity, has remained an unexplored topic in fluid simulation. Existing simulation methods can neither track the evolution of a moving contact line on a deformable surface nor solve the coupling dynamics governed by multiple surface stresses. The lack of these tools makes the simulation of scenes involving contact, wetting, adhesion, capillarity, and elasticity a challenging problem.

To address these challenges, we propose a new computational method that tackles the contact-line dynamics as well as its coupling between surface-tension liquids and elastic deformables. To model the contact-line geometry, we devised a novel Lagrangian representation based on a codimension-one level set on a deformable surface. To solve the contact-line physics, we developed an accurate surface-stress model and its two-way coupling framework to co-evolve the liquid, deformable solid, and their T-junctions. Our model unifies the treatment of the previously separated hydrophobic and hydrophilic fluids in one framework, which facilitates a multitude of small-scale surface-tension phenomena that were difficult to solve.

Our technical contributions can be summarized as follows:

- An interfacial force model that unifies hydrophobic and hydrophilic coupling;
- A codimension-one level set method as well as its Lagrangian representation to track the contact-line evolution on a deformable solid surface;
- A monolithic coupling framework that can handle the force and momentum exchange at the triple junctions of liquid, solid, and air;
- A Newmark-type integration scheme that can reproduce a variety of small-scale elastocapillary phenomena driven by the interactions between surface tension and elasticity.

2 RELATED WORK

Solid-Fluid Interaction. Following the pioneering work on simulating two-way solid-fluid interaction in computer graphics [Carlson et al. 2004; G enevaux et al. 2003; Guendelman et al. 2005], a series of coupling systems have been developed on a dynamic mesh [Klingner et al. 2006], height field [Wang et al. 2007], grid [Robinson-Mosher et al. 2008], particles [Akinci et al. 2012], or their hybrid

[Hu et al. 2018]. Although various two-way coupling methods for Eulerian fluids and Lagrangian solids have been proposed, most focus on large-scale effects and neglect the interfacial stresses of both fluid and solid. Rigorous elastocapillarity modeling in computational physics usually targets the simplest phenomena like the contact between a static droplet and a bulk substrate [Bostwick et al. 2014; Fagbemi et al. 2020; Van Brummelen et al. 2016], which are typically not scalable and produces inconspicuous visual effects. Fei et al. [2017] studied the cohesive behavior of liquid bridges between hair strands, which pioneered the simulation of elastocapillarity in graphics. Ruan et al. [2021] developed a three-way coupling framework with a surface membrane to accurately handle surface tension effects. However, their method only considered hydrophobic rigid bodies. A unified coupling framework that considers body momentum exchange and contact-line dynamics is needed to simulate small-scale interfacial phenomena driven by different wetting properties.

Surface Tension. Surface-tension flow, such as droplets, soap bubbles, and foams, have received extensive attention in computer graphics and computational physics (see [Colinet et al. 2001] and [Popinet 2018] for an overview). A broad range of numerical methods for simulating surface-tension fluid have been invented using grids [Cao et al. 2019; Zheng et al. 2009], particles [Morris 2000; Tartakovsky and Meakin 2005; Wang et al. 2021], meshes [Batty et al. 2012; Da et al. 2015; Zhu et al. 2014], and hybrid Eulerian-Lagrangian frameworks [Hyde et al. 2020; Schroeder et al. 2012; Zheng et al. 2015]. These numerical approaches have facilitated a multitude of physically-based animations on the phenomena of droplets [Da et al. 2016a], bubbles [Busaryev et al. 2012], foam [Ishida et al. 2017], fluid sheets [Th urey et al. 2010], splashes [Zhu et al. 2015] and chains [Wang et al. 2020], as well as solid-fluid contact [Ruan et al. 2021], all of which are driven by strong surface tension on a liquid interface. The Marangoni effect, caused by the unevenly distributed surfactant ratio on the surface, has also recently received attention in graphics simulations by facilitating a series of visually intriguing flow phenomena including tears of wine [Chen et al. 2021] and membrane turbulence [Huang et al. 2020]. Despite these impressive simulation effects, most previous studies focused only on fluid-air interfaces and their interaction with a rigid boundary. Limited research considered the evolution of dynamic junctions among liquid, air, and deformable solids, hindering the numerical modeling of small-scale flow phenomena consisting of surface-tension-dominant liquid and deformable objects.

Elastocapillarity. Elastocapillary phenomena involving elastic deformation in bulk coupled with capillary effects on the liquid surfaces can be observed in a diversity of fields, ranging from biological systems [Flynn and Bush 2008; Heil and White 2002] to nanotechnologies [Mastrangelo and Hsu 1993; Van Spengen et al. 2002]. A range of behaviours of elastic materials induced by capillary forces have been observed in wetting ridge [Karpitschka et al. 2015], adhesion [Cao et al. 2014], self-assembly [Vandewalle et al. 2020], buckling [Cohen and Mahadevan 2003], wrinkling [Huang et al. 2007], and crease [Liu et al. 2019]. Recent technological progress in microfabrication and biomimetic design toward advanced materials has motivated numerous studies of the coupling between surface

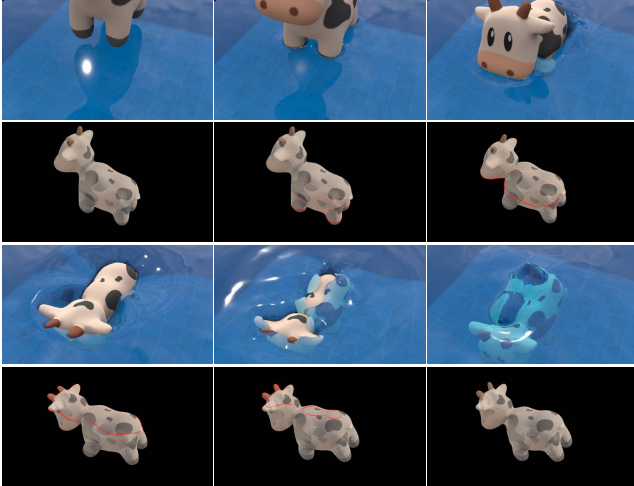


Fig. 2. The evolution of the contact line (red) from emerging to vanishing when a soft cow falls and sinks into a tank of water.

tension and elasticity. Bico et al. [2018] provides a general view of elastocapillarity on three main configurations characterized by dimensions. Some more specific reviews have been dedicated to the coalescence of plates and pillars [Wei et al. 2015], bundling of arrays of fibers [Duprat and Shore 2015; Legrain et al. 2016], and the collapse or folding of microstructures [Crane et al. 2013; Leong et al. 2010]. Theory-wise, Binysh et al. [2021] developed a continuum theory for 3D soft solids experiencing active surface stresses. Singh et al. [2014] presented a fluid-mechanical model of elastocapillary coalescence. Simulation-wise, numerical studies focusing on some specific phenomena have been investigated, such as the deformations of 3D bulk solids under surface tension [Bueno et al. 2018], as well as 1D rods and fibers [Fei et al. 2017; Lecrivain et al. 2020]. However, simulating capillary-induced deformations of thin plates featured by out-of-plane bending is still absent.

Hydrophobicity/Hydrophilicity. The degree to which a surface either attracts or repels water can be termed the hydrophilicity or hydrophobicity of that surface, respectively. Inspired by the famous self-cleaning effect exhibited by the lotus leaves [Barthlott and Neinhuis 1997; Neinhuis and Barthlott 1997], research works on surfaces with special wettability, repellency, and controllable adhesion have been extremely popular [Dalawai et al. 2020; Nishimoto and Bhushan 2013; Sethi and Manik 2018], with applications such as drop-wise condensation, self-cleaning, and oil-water separation [Bixler and Bhushan 2014; Liu and Jiang 2012; Zhang and Seeger 2011]. Static and dynamic contact angle measurements are commonly adapted to study the wetting properties of the surfaces [Yuan and Lee 2013]. Normally, we define a surface as hydrophobic when its static water contact angle θ is greater than 90° , and hydrophilic when θ is less than 90° . Numerical analyses of wettability have been focused on the factors that control the contact angle [Evans et al. 2019], such as the surface roughness [Li et al. 2021], surface chemistry [Kaggwa et al. 2012], and hydrodynamic conditions [Eggers and Stone 2004]. Simulations of wetting effects

and contact angles in computer graphics started from Wang et al. [2005]’s pioneering work on the virtual surface method. Da et al. [2016b] modeled the triple junction by a least-square fitting of an over-determined system. Studies of the interactions with contacting solids have been dedicated to hairs [Fei et al. 2017; Lee et al. 2018, 2019; Rungjiratananon et al. 2012] and fabric cloths [Fei et al. 2018; Huber et al. 2011]. Some recent particle-based approaches include using an SPH model for multi-interaction applications [Yang et al. 2017] and an MPM discretization of surface tension forces with spatial gradients [Chen et al. 2021], which successfully simulated different contact angles and wetting effects.

3 PHYSICS MODEL

3.1 Fluid

We solve the incompressible Navier–Stokes equations to describe the fluid motion:

$$\begin{cases} \frac{\partial \mathbf{u}}{\partial t} + (\mathbf{u} \cdot \nabla) \mathbf{u} = -\frac{1}{\rho} \nabla p + \nu \nabla^2 \mathbf{u} + \mathbf{g}, \\ \nabla \cdot \mathbf{u} = 0, \end{cases} \quad (1)$$

where \mathbf{u} is velocity, ν is the kinematic viscosity, \mathbf{g} is gravity, and p and ρ are fluid pressure and density. Boundary conditions include the no-penetration condition $\mathbf{u} \cdot \mathbf{n} = 0$ on a wall boundary and the Dirichlet boundary constraint $p = 0$ on the free surface. Since surface tension acts only at the free surface, it does not appear in the Navier–Stokes equations but rather enters through boundary conditions. For a free surface with uniform surface tension Υ , the tangential stress is zero because there is no local surface tension gradient. The normal stress must be balanced by the curvature force associated with the surface tension: $\mathbf{n} \cdot \mathbf{T} \cdot \mathbf{n} = \Upsilon (\nabla \cdot \mathbf{n})$, where $\mathbf{T} = -p\mathbf{I} + \rho\nu(\nabla\mathbf{u} + (\nabla\mathbf{u})^T)$ is the stress tensor.

3.2 Solid

We model elastic solid dynamics in their Lagrangian form as:

$$\rho_s \frac{D^2 \mathbf{u}_s}{Dt^2} = \nabla \cdot \boldsymbol{\sigma} + \rho_s \mathbf{g}, \quad (2)$$

where \mathbf{u}_s is the displacement vector, ρ_s is the solid density, $\boldsymbol{\sigma}$ is the elastic stress tensor, and \mathbf{g} is the body force. The elastic body is coupled with the fluid system in terms of both momentum exchange in contact areas and interfacial forces on contact lines.

3.3 Contact Line

Contact-line geometry. A contact line forms when a liquid surface meets a solid object, where three types of surface stresses (liquid-air stress, liquid-solid stress, and solid-air stress) jointly act on the wetting ridge. Geometrically, contact lines located at the tip of the triple junction can be viewed as points in 2D and curves lying on substrate surfaces in 3D. More accurately, a contact-line point or segment should represent a small neighboring volume whose motion is dominated by both volume and surface stresses. Figure 3 shows a contact-line cross-section, with the contact point marked in pale green and its associated control volume enclosed by dashed lines. Because liquid, solid, and air mix around the contact line, its mass

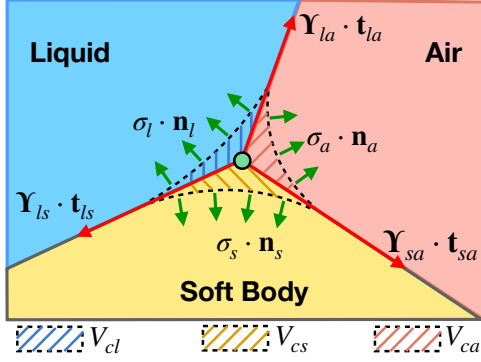


Fig. 3. A microscale view of a contact-line point between a drop and a soft solid, showing the control volume where both interfacial forces and bulk stresses act.

is an integral of these substances' densities in the control volume:

$$m_c = \int_{V_c} \rho_c dV = \int_{V_{cl}} \rho_l dV + \int_{V_{cs}} \rho_s dV + \int_{V_{ca}} \rho_a dV, \quad (3)$$

where ρ_c , V_c are the virtual density and control volume of contact point c and ρ_i is the density of phase i . Here we assume all phases are immiscible and therefore can further write the mass as the sum of integration in each phase, with V_{cl} , V_{cs} , and V_{ca} as their control volume in separate. In practice, we ignored ρ_a since we are using a free surface assumption and do not explicitly model the air.

Contact-line dynamics on a deformable surface. For a deformable solid with $\Upsilon/E \geq w$, where E is Young's modulus, and w is the area over which the line force is spread out, motions will occur due to the unbalanced force between the bulk and surface stresses, and significant deformations will happen at the contact line, as shown in Figure 3. The contact line motion is governed by:

$$m_c \frac{Dv_c}{Dt} = \underbrace{\int_{w_l} \sigma_l \cdot \mathbf{n}_l dL}_{\text{liquid bulk force}} + \underbrace{\int_{w_s} \sigma_s \cdot \mathbf{n}_s dL}_{\text{solid bulk force}} + \underbrace{\int_{w_a} \sigma_a \cdot \mathbf{n}_a dL}_{\text{air bulk force}} + \underbrace{\Upsilon_{la} \cdot \mathbf{t}_{la}}_{l\text{-}a \text{ tangential force}} + \underbrace{\Upsilon_{ls} \cdot \mathbf{t}_{ls}}_{l\text{-}s \text{ tangential force}} + \underbrace{\Upsilon_{sa} \cdot \mathbf{t}_{sa}}_{s\text{-}a \text{ tangential force}}, \quad (4)$$

where Υ_{ij} is the interfacial stress between phase i and j , σ_s is the elastic stress of material opposing the solid deformation, and σ_l is the liquid stress mainly from the pressure which opposes the volume change. We assume σ_a to be negligible. Here \mathbf{n}_i is the inward normal of phase i near the triple junction, and \mathbf{t}_{ij} is the tangential vector pointing along the i - j interface.

Contact-line dynamics on a rigid surface. When a droplet rests on a rigid substrate, the effective area of the triple junction is infinitesimal, so the balance can be considered on a single point, as shown in Figure 4 bottom. Since there are no bulk stresses involved, Equation 4 can be reduced the Young-Dupr e relation:

$$\Upsilon_{la} \cos \theta = \Upsilon_{ra} - \Upsilon_{lr}, \quad (5)$$

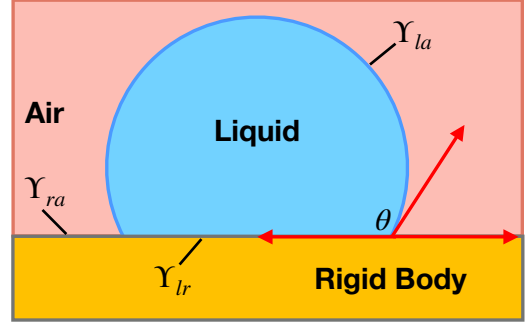


Fig. 4. A drop resting on a stiff solid. The contact angle θ is governed by Young-Dupr e law, which expresses the balance of horizontal projections of the interfacial forces.

where θ is the stable contact angle. This equation holds true if the gas phase is replaced with another immiscible liquid.

In the rest of this paper, we use scalar Υ instead of $\mathbf{\Upsilon}$ to represent the surface stresses by assuming the stress tensor is isotropic. For the liquid-air interface, surface stress scalar and surface energy are termed equivalent to surface tension.

4 DISCRETIZATION

4.1 Fluid

We discretize the fluid volume on a standard marker-and-cell (MAC) grid, where velocities and pressures are stored in a staggered fashion. We employ the advection-projection scheme [Fedkiw et al. 2001; Foster and Fedkiw 2001] by applying the semi-Lagrangian advection, surface tension, viscosity, and gravity force sequentially before the projection step. Viscosity is optional in our implementation, but it can be employed to accelerate the liquid stabilization.

We track the liquid's free surface implicitly using a level set (ϕ) [Sethian and Smereka 2003]. Surface tension is treated in a semi-implicit way [Zheng et al. 2009] to handle high surface-tension fluids at moderate time steps robustly. The key idea is to diffuse the sharp changes of interfacial velocities into a narrowband ε across the surface by solving a Poisson's equation on narrowband velocities:

$$\frac{\mathbf{u}^{\text{new}} - \mathbf{u}^{\text{old}}}{\Delta t} = \underbrace{-\Upsilon \delta(\phi) \kappa \mathbf{n}}_{\text{explicit force}} + \underbrace{\Upsilon \delta(\phi) \Delta t (\nabla^2 \mathbf{u}^{\text{new}})}_{\text{implicit Laplacian}}, \quad (6)$$

where Υ is the interfacial tension that varies at different interfaces, as shown in Figure 5. \mathbf{n} is the unit surface normal ($\mathbf{n} = \nabla \phi / \|\nabla \phi\|_2$) and κ is the mean curvature ($\kappa = \nabla \cdot \mathbf{n}$), both obtained from the liquid level set. $\delta(\phi)$ is a delta function defined within the narrowband ε to the surface as $\delta(\phi) = \frac{1}{2\varepsilon} (1 + \cos(\frac{\phi\pi}{\varepsilon}))$. In our examples, ε is set as $3\Delta x$. This step relieves the time-step restriction by adding surface diffusion proportional to the surface tension strength in the ε -interface with a standard Laplacian.

We employ two types of surface tension, as shown in Figure 5, including Υ_{la} and Υ_{ls} on the liquid-air and liquid-solid interfaces split by the contact lines. To decide the surface tension-type of a grid face at position \mathbf{x} within the narrowband, we find the closest point on the interface by $\mathbf{x}_\phi = \mathbf{x} - \phi(\mathbf{x})\mathbf{n}$ and use the tension parameter

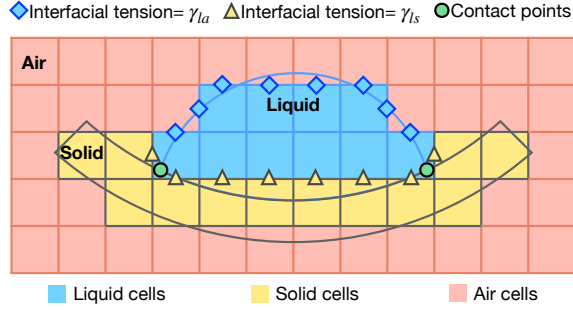


Fig. 5. Discretized cell types are colored blue (liquid), yellow (solid), and red (air). Liquid surface with different tension coefficients is marked by a triangle (liquid-solid interfacial tension) and diamond (liquid-air interfacial tension). Surface stresses at the solid-air interface are ignored.

associated with the surface point's dual cell. We assume Υ_{sa} to be negligible on solid-air interfaces compared to elasticity and did not model it. Please note that this assumption does not hold for ultra-soft materials such as elastomers and hydrogels; they are out of scope of this paper. At the contact line, all three surface stresses accurately model the dynamics in the vicinity of triple junctions. We provide details on calculating the junction forces in Section 4.3.

4.2 Solid

We discretize a solid object on a volumetric mesh (triangle mesh in 2D and tetrahedral mesh in 3D). The mesh resolution is set finer than the background grid (1.5x in our experiments). For time integration, we adapt the semi-implicit integration method proposed by Bridson et al. [2002] by separating the treatments of displacement-induced force $\mathbf{f}_{s,q}$ (e.g. elasticity) and velocity-induced force $\mathbf{f}_{s,v}$ (e.g. damping). The momentum conservation equation can thus be written as:

$$(\mathbf{M}_s - \Delta t \frac{\partial \mathbf{f}_{s,v}}{\partial \mathbf{v}_s}) \mathbf{v}_s^{n+1} = \mathbf{M}_s \mathbf{v}_s^n + \Delta t \mathbf{f}_{s,q}(\mathbf{q}_s^n) + \Delta t \mathbf{g}, \quad (7)$$

where elasticity is handled explicitly, and damping is handled implicitly. For the rest of this paper, we'll use a simplified general form: $(\mathbf{M}_s - \Delta t \mathbf{D}_s) \mathbf{v}_s^{n+1} = \mathbf{M}_s \mathbf{v}_s^n + \Delta t \mathbf{l}_s^n$, where \mathbf{D}_s is the coefficient matrix for the implicit integrated forces, and \mathbf{l}_s corresponds to the rest of the explicitly integrated forces. We omit the derivatives of the force differentials since they have been well studied in previous literature (e.g. [Sifakis and Barbic 2012]).

4.3 Contact Line

4.3.1 Contact-line geometry. The contact line's geometric discretization consists of three key steps: codimension-1 level-set generation, level-set-to-mesh conversion, and mass lump, as briefed in Figure 6. The key idea is to first generate a level-set representation on the solid mesh and then convert it to a Lagrangian mesh. In particular, we first calculate a codimension-1 level set on the deformable solid surface according to the contact between the codimension-0 liquid level set and the codimension-1 solid surface mesh. We devised a novel "enlarge-and-shrink" process to ensure the level set's temporal consistency. Next, we use this codimension-1 level set to calculate a codimension-2 simplicial mesh of segments in 3D and dots in 2D.

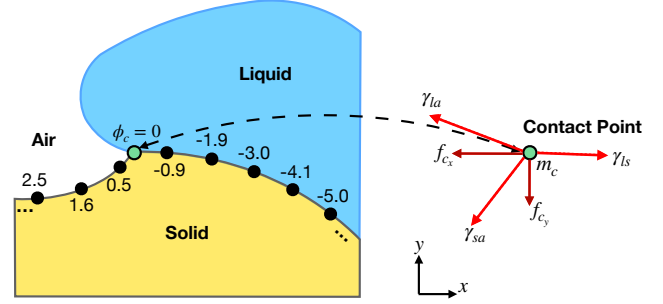


Fig. 6. Left: The codimension-1 level set (ϕ_c) to the contact line on the surface vertices of the solid. Vertices with $\phi_c > 0$ lie at the solid-air interface. Vertices with $\phi_c < 0$ lie at the liquid-solid interface. Contact points (marked by green) exist on edges whose incident vertices have opposite geodesic signs. Right: The three interfacial tensions (Υ) applied to the contact point (m_c) and the resultant axial forces (\mathbf{f}_c).

After generating the Lagrangian representation, we calculate the mass of each mesh vertex by lumping the fluid and solid masses in the surrounding grid cells. We detail each step as follows.

Level set on mesh. Because the evolution of a contact line is always constrained on the deformable solid's surface, we choose to generate a codimension-1 level set (ϕ_c) on the surface to first obtain an implicit representation of the intersection between the liquid and solid. As shown in Figure 7, our procedure takes a codimension-0 (volumetric) level set for liquid surface and a surface mesh for solid surface as input and generates a codimension-1 level set on the solid surface to feature the contact line. Due to the discretization resolution limit, it is challenging to detect the contact between the zero level set of the liquid volume and the mesh surface in a precise and temporally consistent manner. For example, a mesh vertex can happen to be inside or outside a liquid level set due to the linear interpolation of the level-set values within grid cells, which will cause temporally inconsistent results between time frames. We solved this issue by applying a simple "enlarge-and-shrink" mechanism: We first enlarge the liquid level set by a small offset ϵ in the volumetric space. Then, we detect the intersection between this enlarged level set and the solid mesh to generate a mesh level set on the solid surface. Last, we shrink the generated level set by the same offset ϵ on the surface only to obtain the codimension-1 contact line. We illustrate the algorithm workflow in Figure 7 and the steps in Algorithm 1. We note that the generated contour is an approximation to the real contact line because the shortest distance from the mesh vertices to the liquid is not necessarily aligned with the solid surface. We chose ϵ to be the grid size Δx in our experiments. Generally speaking, a larger ϵ generates a smoother contour but further away from the real junction at the high curvature region. A smaller ϵ makes the contour bumpier but closer to the real contact line. We find $\epsilon = \Delta x$ to be a good compromise in practice for two reasons. First, the existence of the surface tension tends to smooth the fluid surfaces with high curvature. Second, when the contact is at a sharp angle, the level-set representation fails to capture it on a sub-cell level (it will produce a rounded arc instead), which causes an (inwardly) underestimation of the T-junction location. Our estimation

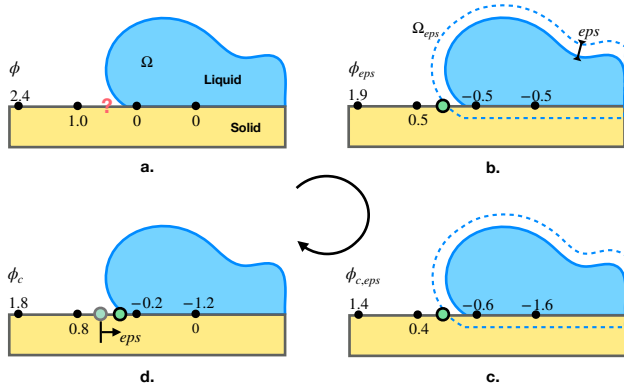


Fig. 7. From a to d: steps to construct the approximate contact line and geodesics on mesh vertices based on the "enlarge-and-shrink" mechanism.

strategy alleviates this error to some extent. In the end, it's easy to find that as the grid resolution scales up to infinity, the liquid level set can represent arbitrarily high curvature and ϵ approaches zero. Thus, the approximated contact line converges to the actual contact line. A convergence analysis is conducted to learn the effect of the resolution on the contact line and system dynamics, as shown in Section 7.1

Algorithm 1 Contact-line Generation

- 1: **Input:** liquid level set ϕ , solid surface mesh.
- 2: **Output:** mesh level set ϕ_c .
- 3: **for** each vertex on solid surface **do**
- 4: Update the level set value: $\phi_{eps} = \phi - \epsilon$
- 5: **end for**
- 6: Reinitialize the mesh level set: $\phi_{eps} \rightarrow \phi_{c,eps}$
- 7: **for** each vertex on solid surface **do**
- 8: Update the level set value: $\phi_c = \phi_{c,eps} + \epsilon$
- 9: **end for**

Reinitialization. We implement a mesh-based fast-marching algorithm to reinitialize the level set on the solid mesh. In particular, we solve the Eikonal equation [Evans 2010] on a mesh to approximate the geodesic distances on a curved domain [Kimmel and Sethian 1998]. We use the simplest planar front approximation to compute geodesics in fast marching by assuming that within a single triangle, the distance function is well-approximated by one whose level sets are straight lines. A detailed implementing instruction can be found at [Bronstein et al. 2008] and [Zhu et al. 2015]. For acceleration, we only reinitialize the level set within a $5\Delta x$ narrow band.

Lagrangian representation. After obtaining a level set on the solid mesh, we extract the codimension-2 Lagrangian representation from it using marching triangles [Lorenson and Cline 1987] in 3D (or marching segment in 2D). A contact-line particle is detected when the two incident vertices of an edge have level set values of opposite signs. Then, we perform a mesh topological repair process [Zhu et al. 2014] to improve the discretization quality by removing the ill-conditioned mesh elements, as illustrated in the inset figure.

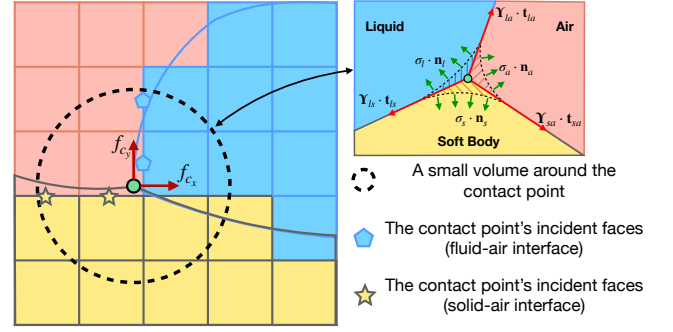


Fig. 8. Incident faces to the contact point marked by stars (solid-air interface) and polygons (fluid-air interface). The effective range of the interfacial forces at the contact point is approximated by a circle. Combined forces (f_{cx}, f_{cy}) will act on the incident faces in the same directions. Forces applied to the solid-air interface will act on the solid vertices incident to the face through the mapping W_s .

In particular, we use two types of operations detailed by [Brochu and Bridson 2009]: split long edges by subdividing all edges with lengths greater than the pre-defined maximum edge length, and collapse short edges by deleting all edges with lengths less than the pre-defined minimum edge length, then replace the edge with a single vertex. The pre-defined maximum and minimum edge lengths are set to be $1.5x$ and $0.5x$ the averaged edge length of the original mesh. The final output is segment meshes to discretize contact lines in 3D and discrete points in 2D.

Mass lumping. After generating the Lagrangian mesh, we calculate the mass for each mesh vertex. As discussed in Section 3.3, each contact point has its associated control volume. As shown in Figure 8, we use a circle centered at the contact point with radius \mathcal{R} in 2D and use a sphere around each segment vertex in 3D. The mass of a discrete contact point is thus calculated as the summation of mass from each cut-cell occupied by phase i . By default, we initialized a small intrinsic mass $m_c^0 = 1e^{-2}\rho\Delta x^2$ for each contact point to avoid any zero mass for numerical robustness. In sum, the lumped mass for each Lagrangian point is calculated as $m_c = m_c^0 + \sum_{r=0}^{\mathcal{R}} \rho_i V_{ci}$.

4.3.2 Contact-line physics. After obtaining the contact line's geometric representation and its mass, we discretize the six terms (three bulk forces and three tangential forces) in Equation 4 to solve its dynamics. As mentioned before, we ignore the air phase, so the air bulk force is zero. The liquid bulk stress is from the pressure which resists volume change, and the solid bulk stress is the elasticity opposing solid deformation. Next, we discuss the calculation of the three interfacial forces $Y_{ij}t_{ij}$.

Tangential direction fitting. The main challenge of calculating the interfacial force between two phases lies in approximating the force direction on each contact-line vertex based on its local geometry. To solve the problem, we fit three tangential directions along the $i - j$ interface based on the local mesh and level-set geometries by

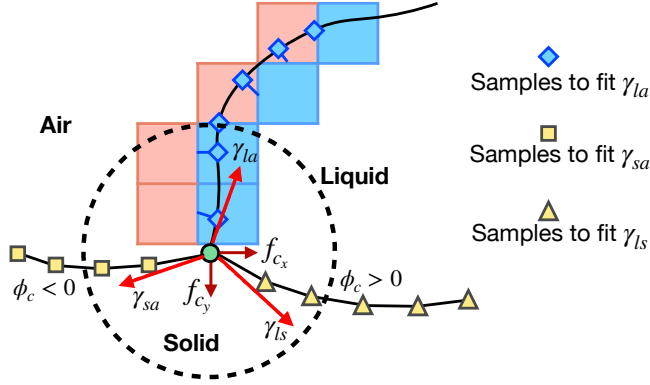


Fig. 9. Sample points on the liquid-air, liquid-solid, and solid-air interfaces to fit the tangential directions of the interfacial tensions.

sampling a set of nearby points on the corresponding interfaces (see Figure 9). Because we have signed geodesics available on the surface mesh from our codimension-1 level set, points on the liquid-solid interface and the solid-air interface can be sampled from the vertices with negative and positive level set values. For sampling points on the liquid-air interface, we first sample nearby fluid-air dual cells on the grid and then find the corresponding closest points on the liquid surface. With samples on each interface, we can fit a plane as well as the normal and tangent of the plane. We use singular value decomposition (SVD) for the numerical implementation of our fitting algorithm. The algorithm to fit the plane, normal, and tangent directions from a group of points $\mathbf{p}_0, \dots, \mathbf{p}_{n-1}$ is summarized in Algorithm 2 by using orthogonal distance regression and SVD. For 2D, we directly use $\mathbf{t} = \mathbf{U}(:, 0)$ as the tangent direction. For 3D, we compute \mathbf{t} use the cross product of the plane normal $\mathbf{n} = \mathbf{U}(:, 2)$ and the local tangent along the contour (\mathbf{t}_c) computed from the neighbouring contact line vertices.

Interfacial force calculation. After getting the tangential vectors, we calculate the interfacial forces as $\gamma_{ij} \mathbf{t}_{ij}$. To couple the calculated force with the Cartesian grid, forces applied to each contact line vertex are projected to the main rectangular axes, as shown in Figure 9. More details on coupling is discussed in Section 5.2.

Algorithm 2 Plane Fitting

- 1: **Input:** Point set $\{\mathbf{p}_0, \dots, \mathbf{p}_{n-1}\}$.
 - 2: **Output:** The best fitted plane.
 - 3: Zero-centering points:
 - 4: $\mathbf{c} = \frac{1}{n} \sum_{i=0}^{n-1} \mathbf{p}_i$,
 - 5: $\mathbf{A} = [\mathbf{p}_0 - \mathbf{c}, \dots, \mathbf{p}_{n-1} - \mathbf{c}]$,
 - 6: Compute the SVD decomposition of \mathbf{A} :
 - 7: $\mathbf{USV}^T = \mathbf{A}$.
 - 8: Extract the plane, normal and tangent from \mathbf{U}
-

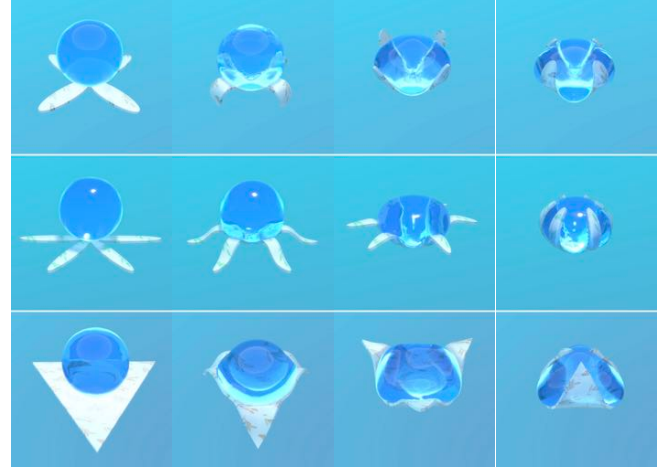


Fig. 10. Wrapping of a droplet with planar solids of different shapes. Top to bottom rows: four petal, six petal, and triangle. Left to right columns: frames 0, 120, 240, and 360.

5 COUPLING SYSTEM

In this section, we introduce our coupling scheme between liquid, solid, and contact-line models. In each time step, we solve two coupling problems: one addressing a conventional solid-fluid coupling problem to predict the system's positions and the other solving a novel solid-fluid-contact-line coupling system for an accurate simulation of the contact-line dynamics. We introduce the details of each of these in the following.

5.1 Solid-Fluid Coupling

The coupling between fluid and solid *without* a contact line largely resembles the framework in [Robinson-Mosher et al. 2008]. We track each grid cell's type (liquid, solid, or air) by checking whether the cell center is inside the liquid's level set or the solid's volumetric mesh, as shown in Figure 5. The coupling happens at the faces sandwiched by a liquid cell and a solid cell. We use an interpolation matrix \mathbf{W}_s to map the velocities and forces between the grid and mesh degrees of freedom (DoFs). For each face whose dual cells have an intersect with the solid's surface, we traverse the intersecting surface elements and sum up the overlapping areas to build the weights of the entries in the corresponding row of \mathbf{W}_s . The overlapping area is approximated by sampling points on the triangle element and computing the portion of points inside the dual cell. The weights of a dual cell are normalized to conserve mass and momentum.

Complementing the pressure projection equation on liquid with $\mathbf{u}^{n+1} = \mathbf{W}_s \mathbf{v}_s^{n+1}$ and substituting the incompressibility condition yields the fluid part of the coupling system:

$$-\frac{1}{\rho} \nabla^2 \hat{p} + \nabla \cdot \mathbf{W}_s \mathbf{v}_s^{n+1} = -\nabla \cdot \mathbf{u}^*, \quad (8)$$

where $\hat{p} = p \Delta t$. To avoid explicitly computing the impulse transfer between liquid and solid, we unify the momentum updates of the solid and nearby liquid by lumping the solid and liquid together.

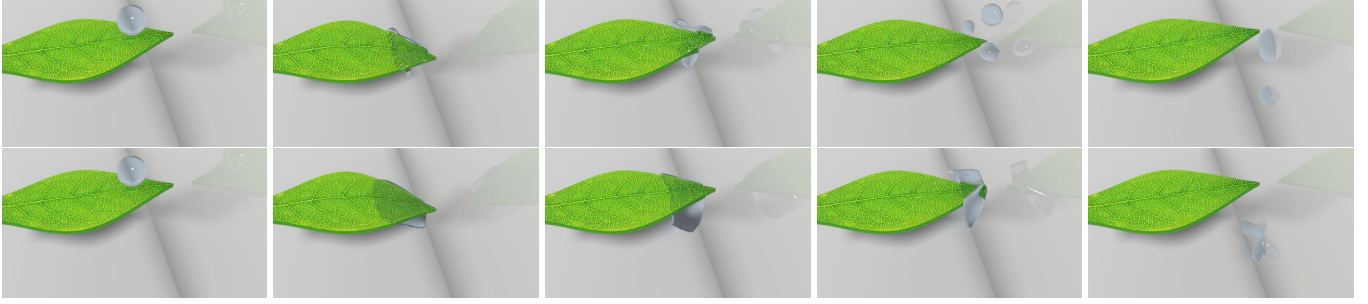


Fig. 11. A droplet splashes down on a hydrophobic (top row) and hydrophilic (bottom row) leaf, then bounces back up to a neutral glass wall (contact angle $\theta = \frac{\pi}{2}$) and rolls down.

The nodal mass matrix after lumping the liquid is:

$$\tilde{\mathbf{M}}_s = \mathbf{M}_s + \mathbf{W}_s^T \mathbf{M}, \quad (9)$$

where \mathbf{M} is a diagonal matrix constructed with the liquid mass in each dual cell, which can be approximated by the liquid level set. The combined momentum update of the solid with the lumped liquid is:

$$(\tilde{\mathbf{M}}_s - \Delta t \mathbf{D}_s) \mathbf{v}_s^{n+1} + \mathbf{W}_s^T V \nabla \hat{p} = \mathbf{M}_s \mathbf{v}_s^* + \mathbf{W}_s^T \mathbf{M} \mathbf{u}^*, \quad (10)$$

where V is the volume of a dual cell and $V \nabla \hat{p}$ is the impulse across the dual cell driven by the pressure difference. \mathbf{v}_s^* is the solid intermediate velocity after integrating all explicit solid forces. \mathbf{u}^* is the liquid intermediate velocity before projection. Combining Equation 8 and Equation 10 yields the two-way solid-liquid coupling system:

$$\begin{bmatrix} -\frac{V}{\rho} \nabla^2 & V \nabla \cdot \mathbf{W}_s \\ -\mathbf{W}_s^T V \nabla & -\tilde{\mathbf{M}}_s + \Delta t \mathbf{D}_s \end{bmatrix} \begin{bmatrix} \hat{p} \\ \mathbf{v}_s^{n+1} \end{bmatrix} = \begin{bmatrix} -V \nabla \cdot \mathbf{u}^* \\ -\mathbf{M}_s \mathbf{v}_s^* - \mathbf{W}_s^T \mathbf{M} \mathbf{u}^* \end{bmatrix}. \quad (11)$$

5.2 Solid-Fluid-Contact-Line Coupling

Next, we discuss how the contact lines couple with both solid and liquid. As discussed before, the interfacial forces act on a small volume around the contact line. We thus search for the liquid-air interfaces and solid-air interfaces within a radius \mathcal{R} around the contact line, as shown in Figure 8. Forces on the contact line are coupled to the solid and liquid through the incident faces, similar to how solid and liquid couple together. The searching radius \mathcal{R} should be greater than the grid resolution Δx , and we use $\mathcal{R} = 3\Delta x$ for both 2D (256^2) and 3D (192^3) experiments. A proper radius should contain enough sampling points while maintaining locality. In our algorithm, we always ensure at least three points are sampled to fit the direction to ensure accuracy. Degeneracy, when there are fewer samples, can happen in two cases: when the droplet size is too small or a small air cavity appears in a liquid volume. For both cases, we ignore the corresponding interfacial force. For small-sized drops, the fluid level set is already inaccurate, so we consider it unresolvable at this resolution. For a small air cavity, we consider liquid pressure to dominate its behavior. It will either collapse soon or become larger when enough points can then be sampled. Another issue is the fitted tangential direction on non-smooth solid surfaces can be inaccurate (e.g. edge of a cube). However, this does not affect the overall behaviors of our simulations by observation. A parameter study is conducted and shown in Section 7.2, demonstrating the

robustness of our method in handling different radii.

Similar to the solid-fluid coupling, we build mapping matrices \mathbf{W}_c and \mathbf{W}_c^T between the contact line and the grid faces implicitly using hash tables. As in Figure 8, the horizontal force f_{c_x} will influence the fluid's motion through horizontal faces (marked by pentagons), similar to Equation 10. The vertical component f_{c_y} will influence the solid's motion through vertices incident to vertical faces (marked by stars). Suppose the impulse being transferred to solid from the contact line is \mathbf{p} , the updated solid momentum is:

$$\mathbf{M}_s \mathbf{v}_s^* = \mathbf{M}_s \mathbf{v}_s + \mathbf{W}_s^T \mathbf{W}_c \mathbf{p}. \quad (12)$$

Similar to Equation 10, the momentum update of the contact line with lumped mass from the incident liquid-air faces is:

$$\tilde{\mathbf{M}}_c \mathbf{v}_c^{n+1} + \mathbf{W}_c^T V \nabla \hat{p} = \mathbf{M}_c^0 \mathbf{v}_c^* + \mathbf{W}_c^T \mathbf{M} \mathbf{u}^*, \quad (13)$$

where $\tilde{\mathbf{M}}_c = \mathbf{M}_c^0 + \mathbf{W}_c^T \mathbf{M}$. $\tilde{\mathbf{M}}_c$ should be the mass of liquid within the small volume around the contact line. We set the contact point as a small intrinsic mass ($1e^{-2} \rho \Delta x^2$) for robustness. The momentum update of the solid by considering both liquid and contact line is:

$$\begin{aligned} & (\hat{\mathbf{M}}_s - \Delta t \mathbf{D}_s) \mathbf{v}_s^{n+1} + \mathbf{W}_s^T V \nabla \hat{p} \\ & = \mathbf{M}_s \mathbf{v}_s^* + \mathbf{W}_s^T \mathbf{M} \mathbf{u}^* + \mathbf{W}_s^T \mathbf{W}_c \mathbf{M}_c^0 \mathbf{v}_c^n + \mathbf{W}_s^T \mathbf{W}_c \mathbf{f}_c \Delta t, \end{aligned} \quad (14)$$

where $\hat{\mathbf{M}}_s = \tilde{\mathbf{M}}_s + \mathbf{W}_s^T \mathbf{W}_c \mathbf{M}_c^0$. We treat the force at the contact line (\mathbf{f}_c) explicitly here. The complete coupling equations including all terms are:

$$\begin{aligned} & \begin{bmatrix} -\frac{V}{\rho} \nabla^2 & V \nabla \cdot \mathbf{W}_s & V \nabla \cdot \mathbf{W}_c \\ -\mathbf{W}_s^T V \nabla & -\hat{\mathbf{M}}_s + \Delta t \mathbf{D}_s & \\ -\mathbf{W}_c^T V \nabla & & -\tilde{\mathbf{M}}_c \end{bmatrix} \begin{bmatrix} \hat{p} \\ \mathbf{v}_s^{n+1} \\ \mathbf{v}_c^{n+1} \end{bmatrix} \\ & = \begin{bmatrix} -V \nabla \cdot \mathbf{u}^* \\ -\mathbf{M}_s \mathbf{v}_s^* - \mathbf{W}_s^T \mathbf{M} \mathbf{u}^* - \mathbf{W}_s^T \mathbf{W}_c \mathbf{M}_c^0 \mathbf{v}_c^* \\ -\mathbf{M}_c^0 \mathbf{v}_c^* - \mathbf{W}_c^T \mathbf{M} \mathbf{u}^* \end{bmatrix}. \end{aligned} \quad (15)$$

where \mathbf{v}_c^* is the intermediate velocity of the contact line after integrating the interfacial forces.

6 TIME INTEGRATION

We introduce our Newmark-type time integration scheme in this section. In each time step, we first compute the mid-point solid velocity, which is then used to update the solid position. Next, we compute the liquid advection velocity using the updated solid position as boundaries, which is used to update the free surface. Finally,

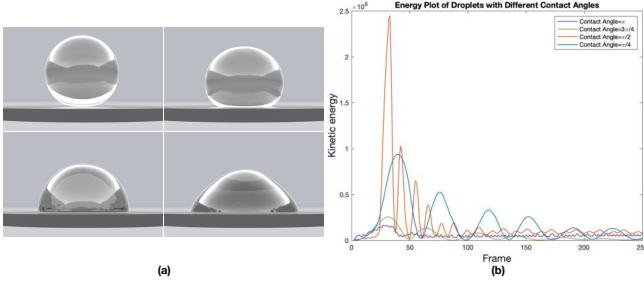


Fig. 12. (a): Static contact angles formed by liquid drops resting on rigid surfaces. From upper left to bottom right, the angles are approximately 180, 135, 90, and 45 degrees. (b): Kinetic energy evolution of each case.

the contact line is constructed at the new positions, and velocities are updated accordingly. The position updates resemble the standard two-way coupling scheme, while the velocity update involves coupling to the contact line. The concrete advancing algorithm can be described by the following steps.

- (1) Integrate the gravity and diffusion terms to fluid velocity, and all explicit solid forces (gravity and elasticity) for half time step:

$$\begin{cases} \mathbf{u}^{n+\frac{1}{2}} = \mathbf{u}^n + \frac{\Delta t}{2} (\nu \nabla^2 \mathbf{u}^n + \mathbf{g}), \\ \mathbf{v}_s^{n+\frac{1}{2}*} = \mathbf{v}_s^n + \frac{\Delta t}{2} \frac{\mathbf{I}_s^n}{M_s}. \end{cases} \quad (16)$$

- (2) Solve Equation 11 for the two-way coupling system to get $\mathbf{v}_s^{n+\frac{1}{2}}$. Update the solid positions for one time step. Revert the fluid velocity to time n :

$$\begin{cases} \mathbf{x}_s^{n+1} = \mathbf{x}_s^n + \Delta t \mathbf{v}_s^{n+\frac{1}{2}}, \\ \mathbf{u} \leftarrow \mathbf{u}^n. \end{cases} \quad (17)$$

- (3) Compute the solid effective velocity using the position change, then revert the solid velocity to time n :

$$\begin{cases} \mathbf{v}_s^{\text{eff}} = \frac{\mathbf{x}_s^{n+1} - \mathbf{x}_s^n}{\Delta t}, \\ \mathbf{v}_s \leftarrow \mathbf{v}_s^n. \end{cases} \quad (18)$$

Similar to [Guendelman et al. 2005], we project \mathbf{u}_n by solving a standard fluid Poisson's equation using the mapped solid effective velocity ($\mathbf{W}_s \mathbf{v}_s^{\text{eff}}$) as Neumann boundary conditions. A volume correction term is added to the right-hand side of Poisson's equation. The resulting velocity is our leak-proof and volume-conservative advection velocity \mathbf{u}^{adv} .

- (4) Update the position of the free surface of the liquid using the advection velocity:

$$\frac{\phi^{n+1} - \phi^n}{\Delta t} + (\mathbf{u}^{\text{adv}} \cdot \nabla) \phi^n = 0. \quad (19)$$

Now positions of both solid and liquid have been updated to $n + 1$. Our next goal is to find the coherent velocities in this new configuration.

- (5) Compute the intermediate fluid velocity by integrating all non-pressure-based terms (advection, gravity, diffusion, and surface

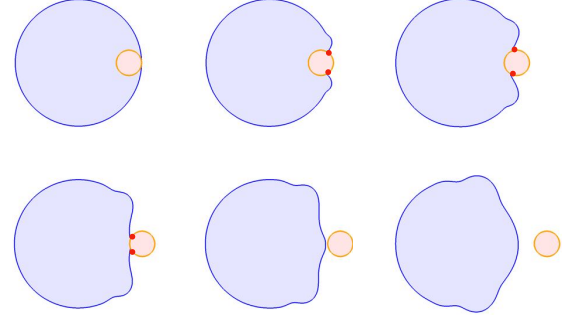


Fig. 13. A hydrophobic rigid sphere escapes from a liquid volume, with contact points marked by red dots sweeping the sphere's surface

tension), and the intermediate solid velocity by integrating all explicit solid forces:

$$\begin{cases} \frac{\mathbf{u}^* - \mathbf{u}^n}{\Delta t} + (\mathbf{u}^{\text{adv}} \cdot \nabla) \mathbf{u}^n = \nu \nabla^2 \mathbf{u}^n + \mathbf{g}, \quad \text{s.t. } \Upsilon \text{ on } \partial \phi^{n+1}, \\ \mathbf{v}_s^* = \mathbf{v}_s^n + \Delta t \frac{\mathbf{I}_s^{n+1}}{M_s}. \end{cases} \quad (20)$$

Both velocity and liquid surfaces are advected using the semi-Lagrangian scheme. Grid cell types are updated at the end.

- (6) Construct the contact line by following Section 4.3 using the update solid and liquid positions (\mathbf{x}^{n+1} , ϕ^{n+1}). Integrate the interfacial tensions explicitly to the contact line:

$$\mathbf{v}_c^* = \mathbf{v}_c^n + \Delta t \frac{\mathbf{f}_c^{n+1}}{M_c}. \quad (21)$$

- (7) Solve Equation 15 for the fully-coupled system to get \mathbf{v}_s^{n+1} , as well as the pressure to project the intermediate fluid velocity (\mathbf{u}^*) to be divergence free (\mathbf{u}^{n+1}).

7 RESULTS

We first conduct validation experiments and compare our approach with other related works. Next, we showcase several simulations to highlight our approach's capability in unifying the coupling with different surface stresses and include performance analysis. All the simulations ran on a PC equipped with a 16-core 3.50 GHz CPU and an NVIDIA GeForce RTX 2070 graphics card.

7.1 Validation

We first validate our contact-line tracking algorithm, followed by static contact angles on rigid surfaces. Next, we conduct two independent experiments to verify how our algorithm affects the motions of liquid and solid separately. We compared our approach with the state-of-the-art at the end.

Contact Angles. We show our method capable of simulating various degrees of hydrophobic or hydrophilic behavior as a droplet settles on a rigid surface in Figure 12 (a). We implicitly control the contact angles by manipulating the three surface stresses based on the Young equation (5), $\theta = \arccos(\frac{\Upsilon_{ra} - \Upsilon_{lr}}{\Upsilon_{la}})$. It can be seen that only one of Υ_{ra} and Υ_{lr} is needed in company with Υ_{la} to decide θ , so we

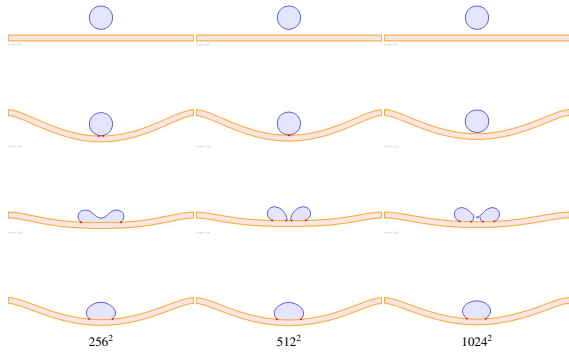


Fig. 14. Simulation of a liquid drop falls to a hydrophobic soft plate in 2D discretized by different resolutions, with contact points marked by red dots.

simply keep $\Upsilon_{ra} = 0$. For 180 degree, we set $\Upsilon_{la} = \Upsilon_{lr} = 3.0$ mN/cm. For 90 degree, we set $\Upsilon_{la} = 2.0$ mN/cm and $\Upsilon_{lr} = 0.0$ mN/cm. For 135 and 45 degrees, we use the same $\Upsilon_{la} = \sqrt{2.0}$ mN/cm but opposite Υ_{la} with an absolute value equal to 1.0 mN/cm. We also plot the changes of the kinetic energy of the droplets in Figure 12 (b). Although we did not employ any type of viscosity, the vibrating droplets tend to stabilize due to numerical dissipation. Please note that the noisy oscillation of the purple curve (Contact Angle = π) is the instability caused by the overlarge surface tension.

Escaping Sphere from a Droplet. We test the tracking accuracy of our contact line in both 2D and 3D. Figure 13 shows the emerging, sweeping, and vanishing of 2D contact points when a hydrophobic sphere initially immersed in liquid escapes. For a hydrophilic sphere, it will stay inside the liquid drop without any movement. Figure 2 shows the reverse process in 3D, where contact lines rendered in red describe the sinking processes of a soft cow. In either case, our algorithm is capable of robustly tracking the contact line without any external interference.

Convergence Analysis. We show the convergence of the contact line and overall system dynamics in 2D, by gradually increasing the resolution of the grid and the solid mesh. Figure 14 shows the evolution of the droplet topology and contact point positions. As the grid resolution increases from 256^2 to 1024^2 , the simulation results converged into a process of droplets breaking into smaller ones and then merging in the end.

Kinematic Sphere in Contact. We test how a liquid will react to a hydrophilic surface by manually moving a rigid sphere inside and outside the liquid, as shown in Figure 17 (a). Since the object is not deformable, we can observe how the contact line affects the motion of liquid through coupling. Traditional two-way solid-fluid coupling methods usually consider pressure as the only coupling media and thus cannot correctly handle the adhesion effect at the triple junction where liquid, solid, and air meet, as shown in Figure 17 (a) right. Our approach can make a distinction in how the liquid responds to hydrophobic or hydrophilic surfaces. In Figure 17 (a) left, the liquid tends to climb on and stick to the hydrophilic surface of the rigid sphere.

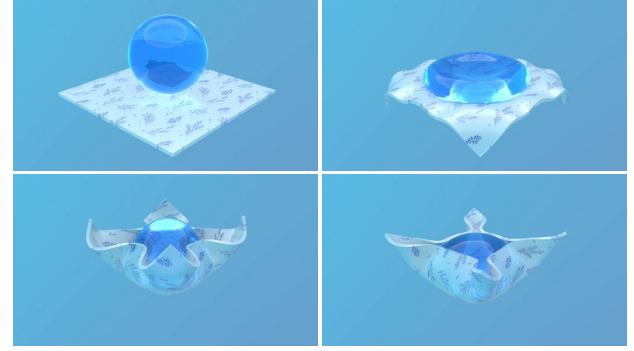


Fig. 15. 3D self-wrapping of a droplet with a square soft membrane, forming a flower shape at the equilibrium state. Frame sequence: upper left (0), upper right (150), central left (300), central right (450), bottom (600).



Fig. 16. Final frame of the capillary origami example using different sampling radii for force fitting. From left to right, the searching radius \mathcal{R} is set to be $2\Delta x$, $3\Delta x$, and $4\Delta x$.

Wrapping Thin Shell on a Droplet. To quantify the effect applied to a solid solely from the contact line, we set up a zero-gravity scene where the solid is initially undeformed and barely in contact with a liquid drop, as shown in Figure 17 (b). In this case, neither gravity nor liquid pressure exists, and thus the only force that can trigger the deformation of a solid is the adhesion exerted by the contact points. Both liquid and solid will remain static by using a traditional two-way coupling method to simulate. Our approach allows realistic wrapping motion with flexible control over the contact angles by changing the relative strengths of the interfacial stresses, as shown in Figure 17 (b).

Comparison to [Ruan et al. 2021]. As discussed in Section 2, previous works in computer graphics rarely emphasize the role of surface stresses in solid-fluid coupling. A related work is done by Ruan et al. [2021], where surface tension of a liquid is employed to support heavy objects. Due to the lack of contact-line treatment, [Ruan et al. 2021] can simulate only hydrophobic phenomena. Our solver extends the scope of simulations from rigid bodies to deformable bodies and from hydrophobic only to both hydrophobic and hydrophilic interactions. We note that most of the examples we show in this paper are beyond the capacity of the solver proposed by Ruan et al. [2021]. We compare our approach to [Ruan et al. 2021] as shown in Figure 17 (c). Under a hydrophobic setting ($\Upsilon_{la} = \Upsilon_{ls} = 1.5$ mN/cm, $\Upsilon_{sa} = 0$), our approach can correctly model the floating behavior of a rigid sphere with two times larger density than the liquid, which is akin to the results obtained by [Ruan et al. 2021]. In addition to the

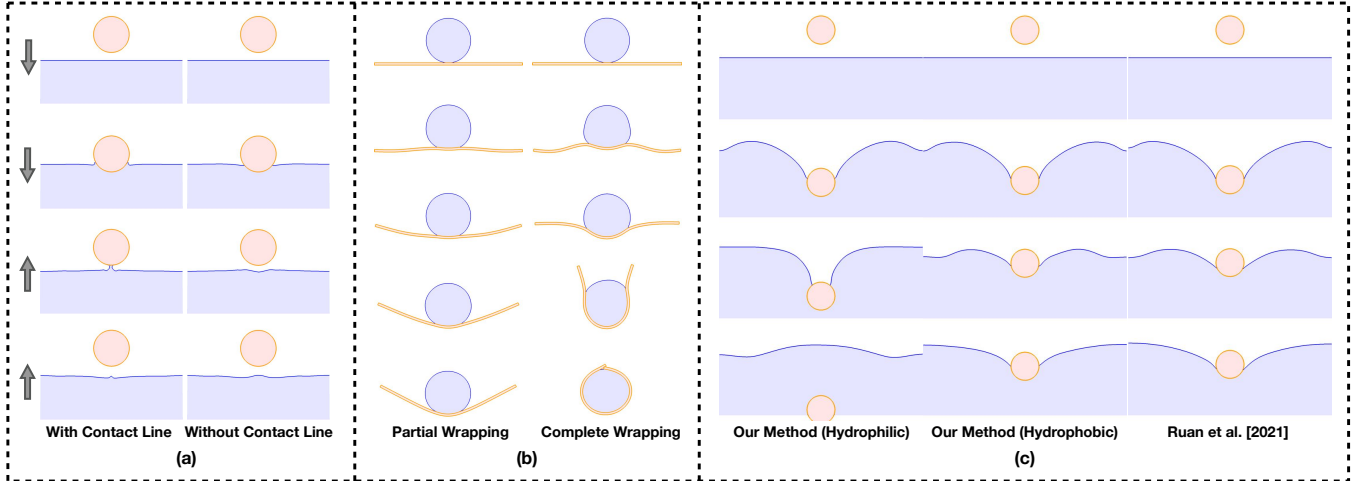


Fig. 17. A series of 2D validation tests. (a): Adhesion effect between liquid and a hydrophilic moving sphere with (left column) and without (right column) modeling and coupling the contact line. (b): 2D wrapping of a droplet with a soft membrane under zero gravity. Different contact angles can be obtained by controlling the interfacial stress relations, forming states ranging from no wrapping to complete wrapping. (c): A comparison between our method and Ruan et al. [2021] at dropping heavy volumetric objects into the water. Our method can produce both floating and sinking scenes at the same liquid-air surface tension by controlling the solid surface properties.

hydrophobic model, our approach can obtain hydrophilic coupling effects by setting $\Upsilon_{la} = \Upsilon_{sa} = 1.5 \text{ mN/cm}$ and $\Upsilon_{ls} = 0$.

7.2 Examples

Capillary Origami. Figure 15 shows a droplet deposited on a thin elastic plate, which bends the plate to minimize the liquid-air interface, leading to the spontaneous wrapping of the droplet. Different shaped planar structures can be folded into various three-dimensional adhesion patterns, as shown in Figure 10. We find our simulation results with triangle and square substrates match well with what scientists observed in experiments [Bico et al. 2018; Py et al. 2007]. In all origami-type examples, we model the solid using the very simple mass-spring model with spring stiffness $k_s = 1e4 \text{ mN/cm}$. The three surface stresses Υ_{la} , Υ_{ls} , and Υ_{sa} are 1.2, 0.2 and 0.5 mN/cm respectively. Both liquid and solid densities are 1 g/cm^3 . Figure 16 shows the parameter study with a varying sampling radius.

Capillary Self-Assembly. Figure 18 shows the self-assembly of a 3D cuboid container by a spherical droplet, starting from a planar elastic cross composed of six pieces. The densities of the droplet and the plate are 1 g/cm^3 and 3 g/cm^3 respectively. The spring stiffness k_s of the solid is $1e5 \text{ mN/cm}$, and the connecting bridges are a third thinner than the main body. The three surface stresses Υ_{la} , Υ_{ls} , and Υ_{sa} are 1.2, 0.1 and 0.6 mN/cm. The bottom face of the central part is fixed, and the other five faces are decorated with triangles, squares, and round holes.

Raindrops on Leaves. Figure 11 compares a leaf-raindrop system with different surface wettability. A systematic experimental study of such a system has been conducted by Gart et al. [2015]. We find the droplet breaks into smaller droplets and rebounds from the non-wettable beam. The wettable beam, on the other hand, keeps in

contact with the droplet until it separates at the leaf apex. To the right is a transparent wall where droplets splash onto and flow down. In this example, the leaf has a spring stiffness of $1e6 \text{ mN/cm}$ and density of 2 g/cm^3 . The three interfacial stresses (Υ_{la} , Υ_{ls} and Υ_{sa}) for the hydrophobic scene (upper row) are 2.0, 0.3 and 0.1 mN/cm. The corresponding values for the bottom hydrophilic scene are 0.1, 0.2 and 1.0 mN/cm. The surface stress of the right wall is selected such that the contact angle is $\frac{\pi}{2}$.

Droplets on Beams. Figure 19 shows droplets impact on cantilever beams at high speed (500 cm/s), causing conspicuous liquid breaking and rebounding. The density of the beam is 2 g/cm^3 , which is two times the liquid drop. In order to enhance the impact, we use a stiff beam material with k_s equal to $4e7 \text{ mN/cm}$. The top row has the largest surface tension ($\Upsilon_{la} = 3.0 \text{ mN/cm}$) and superhydrophobic surface ($\Upsilon_{ls} = 0.8 \text{ mN/cm}$; $\Upsilon_{sa} = 0.0 \text{ mN/cm}$). The middle row has a moderate surface tension ($\Upsilon_{la} = 1.0 \text{ mN/cm}$) and neutral solid surface ($\Upsilon_{ls} = 0.2 \text{ mN/cm}$; $\Upsilon_{sa} = 0.4 \text{ mN/cm}$). The bottom row has the smallest surface tension and hydrophilic surface where Υ_{la} , Υ_{ls} and Υ_{sa} are 0.2, 0 and 0.8 mN/cm respectively. We compare our method with the traditional coupling approach that does not model the contact line using the middle row's setup, where the contact angle is supposed to be $\frac{\pi}{2}$. Figure 20 shows our method correctly reflecting the expected contact angle, while the traditional method fails to distinguish hydrophobic and neutral surfaces.

Floating or Sinking. Figure 21 shows the comparison of thin deformable plates with different surface energies falling into a liquid with different surface tensions. The liquid density remains 1 g/cm^3 and the solid density is 5 g/cm^3 . The solid spring stiffness k_s is $5e3 \text{ mN/cm}$. The upper row has surface stress coefficients of $\Upsilon_{la} = 2.0 \text{ mN/cm}$, $\Upsilon_{ls} = 0.5 \text{ mN/cm}$, and $\Upsilon_{sa} = 0.1 \text{ mN/cm}$. The bottom row has the same surface stress on the liquid-solid interface,



Fig. 18. Self-assembly of a dagger-shaped elastic plate with soft bridge connections placed underneath a liquid drop, forming a cuboid 3D structure at the final state. Frame sequence: upper left (0), upper right (100), central left (200), central right (300), bottom (400).

but Υ_{la} and Υ_{sa} swap. The relative strengths of these parameters decide whether the coupled system tends to minimize the solid-air interface (sinking) or the liquid-air interface (floating).

Droplets on Plates. The goal of this experiment is to compare the contact angles between liquids and moving deformable solids with different surface properties. The rightmost column of Figure 22 shows three representative contact angles when the soft plates come to rest. In this example, the density of the plate is 2.5 g/cm^3 , and the spring stiffness is $5e4 \text{ mN/cm}$. The liquid-air, liquid-solid and solid-air surface stresses for the middle row of Figure 22 are 1.0, 0.1 and 0.1 mN/cm , which form a $\frac{\pi}{2}$ contact angle. For the scenes with contact angles π and 0, the corresponding parameters are 3.0, 0.5 and 0.1 mN/cm and 0.01, 0.1 and 0.5 mN/cm .

7.3 Performance

We summarize in Table 1 the time consumption breakdown in a time step for each of our 3D examples. Most operations are parallelized using OpenMP, including the matrix assembly. We use a standard conjugate gradient solver with a Jacobi preconditioner on GPU to solve linear systems (the solver's convergence tolerance is set as $1e-5$). The main bottlenecks are from the three solves (Section 6 Step 2, 3 and 7). Please note that Equation 11 and 15 are indefinite systems, but we find our solver capable of solving them without compromising the convergence performance. The computational cost of all contact-line-related operations (fast marching, remeshing, force fitting, etc) are marginal compared to the linear solvers. The grid resolution for all 3D examples is 192^3 . Parameters for all examples are discussed in Section 7.2.

8 CONCLUSION

We propose a novel geometric representation that robustly tracks the contact lines between liquid, solid, and air on moving surfaces, which supports the simulation of hydrophobic and hydrophilic elastocapillary systems. We introduce the contact-line dynamics by considering both surface and bulk stresses and how they are discretized on a mixed Eulerian-Lagrangian system. By coupling the

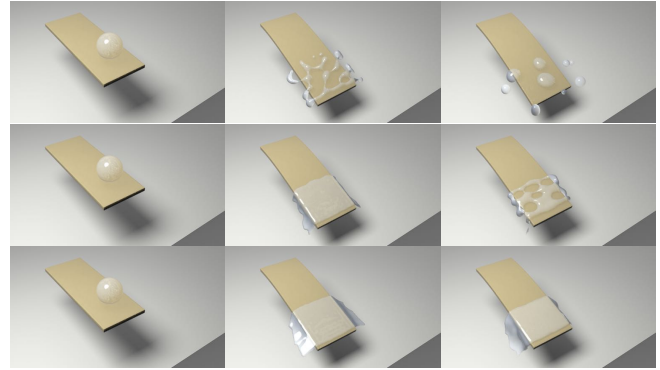


Fig. 19. Falling, splashing, and bouncing of water drops on cantilever beams. Different contact patterns between liquid and beam surfaces can be observed by controlling the relative strengths of the interfacial stresses. From top to bottom row, we have hydrophobic, neutral, and hydrophilic surfaces.

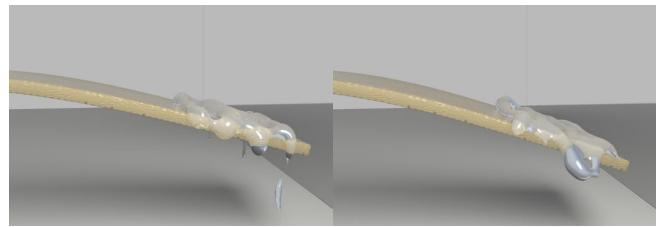


Fig. 20. Side views of a droplet colliding with a neutral surface cantilever beam with (left) and without (right) modeling the contact line.

dynamics of the liquid, solid, and contact line altogether, we are capable of simulating a wide range of phenomena ranging from wetting, splashing, and capillary adhesion to contact angles and elastocapillarity. These examples show that our method naturally handles hydrophobic and hydrophilic solid-liquid interactions based on first principles. We believe resolving dynamics at the multi-phase junctions are critical to exploring more complex phenomena, such as capillary twist, buckling, wrinkles, and instabilities, and also have broad application scopes in surface engineering, material science, and biology.

Limitation. Our approach has three major limitations. First, our contact line model is currently built on codimension-0 volumetric solids and does not support codimension-1 thin shells and codimension-2 threads. This hinders the simulation of many interesting coupling phenomena between surface-tension liquids and extremely thin and curved objects (e.g., droplets on a lotus leaf). When a thin shell penetrates the liquid surface, contact lines on different sides of the shell can be different, which was not considered in our current model and requires proper treatment of the surface mesh's direction. Tackling contact between threads and liquid is more challenging, where the geometric representation degenerates from contact lines to points. Considering both points and curves as general contact geometries are one of our plans. However, detecting contacts between thin filaments and liquid on a grid poses more difficulties and requires further research. Second, the interfacial forces at the contact line

Table 1. Performance Analysis of the 3D Examples per Time Step.

Figure	Scene Description	#Verts	#Elems	CFL	Time Step (s)	1st Solve (s)	2nd Solve (s)	3rd Solve (s)	Total (s)
15	Origami (square)	28,227	92,160	0.7	6.67e-3	0.45	0.39	0.52	4.12
10 (top)	Origami (four petal)	10,628	38,672	0.7	6.67e-3	0.38	0.37	0.42	3.56
10 (mid)	Origami (triangle)	23,313	85,652	0.7	6.67e-3	0.4	0.37	0.45	3.87
10 (bot)	Origami (six petal)	17,886	59,562	0.7	6.67e-3	0.4	0.38	0.42	3.66
21 (top)	Tank (float)	7,605	28,880	0.5	1e-2	1.48	1.52	1.59	9.94
21 (bot)	Tank (sink)	7,605	28,880	1.0	1e-2	1.51	1.58	1.7	10.32
2	Tank (sink cow)	26,069	143,193	1.0	1e-2	2.52	2.65	2.77	16.42
11 (top)	Leaf (hydrophobic)	17,244	70,795	0.5	1.67e-3	0.33	0.30	0.33	3.06
11 (bot)	Leaf (hydrophilic)	17,244	70,795	0.5	1.67e-3	0.31	0.30	0.32	2.96
22 (top)	Contact ($\theta = \pi$)	47,045	184,320	0.7	4e-2	0.36	0.29	0.34	3.38
22 (mid)	Contact ($\theta = \pi/2$)	47,045	184,320	0.7	4e-2	0.34	0.3	0.33	3.35
22 (bot)	Contact ($\theta = 0$)	47,045	184,320	0.7	4e-2	0.32	0.29	0.32	3.59
19 (top)	Beam (hydrophobic)	31,605	122,880	0.5	1.67e-3	0.3	0.28	0.36	3.39
19 (mid)	Beam (neutral)	31,605	122,880	0.5	1.67e-3	0.33	0.29	0.32	3.37
19 (bot)	Beam (hydrophilic)	31,605	122,880	0.5	1.67e-3	0.28	0.31	0.31	3.14
18	Self-Assembly	39,163	117,239	0.7	6.67e-3	0.37	0.36	0.41	3.94

* The material parameters are described in Section 7.2; and the grid resolution for all 3D examples are identical: $\Delta x = 5.2e-2(\text{cm})$.

* What each solve is referring to is discussed in Section 7.3; time for parallel matrix assembly is included.

* Other major time-consuming operations include advection (parallelized), solving implicit surface tension, computing mapping operators (parallelized), and spatial hashing.

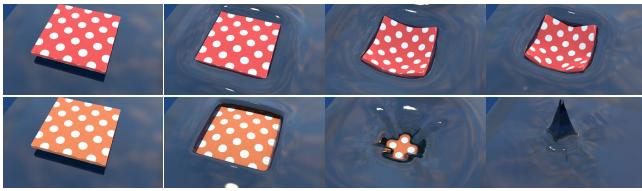


Fig. 21. Falling of a hydrophobic/hydrophilic solid into a tank of liquid with strong/weak surface tension. The density ratio between the solid and the liquid is 5. The top row shows the stable contact between the solid and the curved liquid surface. Strong surface tension enables the liquid to support much denser materials. The bottom row shows the immersion process of a solid sinking into the liquid with low surface tension, causing a high waterspout.

are explicitly applied to the system, due to the challenges in formulating an implicit representation of the force direction based on fitting sample points. As shown in Table 1, we keep the CFL number below 1 in our experiments to ensure stability. An implicit treatment of surface tension across multiple phases to enable large time steps will be an important next step. Third, our current linear solver is not optimal: The convergence of the conjugate gradient solver on an indefinite system (11, 15) is not guaranteed. Building better preconditioners and forming SPD systems for a contact-line problem remains to be explored. Another bottleneck of our solver is the GPU memory, limiting our simulations' scalability toward the centimeter length scale. Due to the complexity of the coupling system, we did not employ a matrix-free paradigm to optimize the performance. Customizing a more efficient solver both in space and time is important to explore more complex, large-scale phenomena.

Future Work. We propose two future directions to explore based on the current work. First, we plan to incorporate more complicated

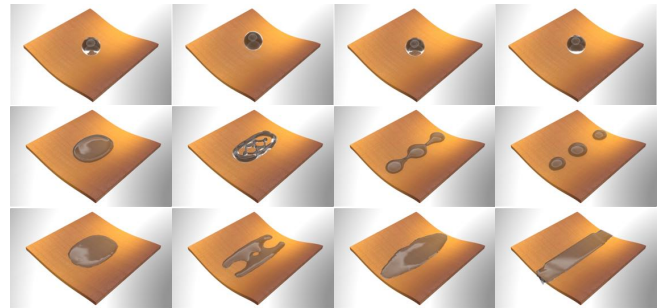


Fig. 22. Different contact angles between a liquid drop and a soft plate can be obtained by varying the ratios between the three interfacial tension coefficients. From top to bottom, the contact angles are around π , $\frac{\pi}{2}$, and 0.

solid sub-systems into the framework. These systems could either manifest complex geometries, such as thin shells and filaments, or exhibit multi-component physics, such as rigid-rigid articulation or rigid-deformable coupling. Simulating surface-tension contact with these novel mechanical systems and materials will not only allow novel animations but also pave the way for their computational optimization and design. Second, a unified framework for handling hydrophobic and hydrophilic coupling opens up possibilities for the visual simulation a new set of natural phenomena, especially the interactions between plants and rain droplets. This work conducted some preliminary research in this direction (see Figure 11), while many interesting and exciting questions remain to be answered by future explorations. For example, what is the relation between the splash shape and the leaf surface? What is the distribution of drop size and pattern due to the leaf's hydrophobicity (e.g., lotus leaf)? Will the microstructural pattern on a solid surface affect the coupling dynamics under a hydrophobic/hydrophilic setting?

At the same time, an accurate surface-aware coupling algorithm will enable the simulation and optimization of a new family of solid-fluid-interaction problems, such as fish swimming, bird flying, and hydrophobic material coating. Answering these questions with novel computational tools will not only enable the production of new visual effects but also pave the way to develop a mechanistic understanding of the intricate physics underpinning these natural phenomena.

ACKNOWLEDGMENTS

We thank all the anonymous reviewers for their constructive feedback. We acknowledge NSF-1919647, 2106733, 2144806, and 2153560 for funding support. We credit the Houdini education license for producing the video animations.

REFERENCES

- Nadir Akinci, Markus Ihmsen, Gizem Akinci, Barbara Solenthaler, and Matthias Teschner. 2012. Versatile rigid-fluid coupling for incompressible SPH. *ACM Transactions on Graphics (TOG)* 31, 4 (2012), 1–8.
- Wilhelm Barthlott and Christoph Neinhuis. 1997. Purity of the sacred lotus, or escape from contamination in biological surfaces. *Planta* 202, 1 (1997), 1–8.
- Christopher Batty, Andres Uribe, Basile Audoly, and Eitan Grinspun. 2012. Discrete viscous sheets. *ACM Transactions on Graphics* 31, 4 (2012), 1–7.
- José Bico, Étienne Reyssat, and Benoît Roman. 2018. Elastocapillarity: When surface tension deforms elastic solids. *Annual Review of Fluid Mechanics* 50 (2018), 629–659.
- Jack Binysh, Thomas R Wilks, and Anton Souslov. 2021. Active elastocapillarity in soft solids with negative surface tension. *arXiv preprint arXiv:2101.04006* (2021).
- Gregory D Bixler and Bharat Bhushan. 2014. Rice-and butterfly-wing effect inspired self-cleaning and low drag micro/nanopatterned surfaces in water, oil, and air flow. *Nanoscale* 6, 1 (2014), 76–96.
- Joshua B Bostwick, Michael Shearer, and Karen E Daniels. 2014. Elastocapillary deformations on partially-wetting substrates: rival contact-line models. *Soft Matter* 10, 37 (2014), 7361–7369.
- Robert Bridson, Ronald Fedkiw, and John Anderson. 2002. Robust treatment of collisions, contact and friction for cloth animation. In *Proceedings of the 29th annual conference on Computer graphics and interactive techniques*. 594–603.
- Tyson Brochu and Robert Bridson. 2009. Robust topological operations for dynamic explicit surfaces. *SIAM Journal on Scientific Computing* 31, 4 (2009), 2472–2493.
- Alexander M Bronstein, Michael M Bronstein, and Ron Kimmel. 2008. *Numerical geometry of non-rigid shapes*. Springer Science & Business Media.
- Jesus Bueno, Hugo Casquero, Yuri Bazilevs, and Hector Gomez. 2018. Three-dimensional dynamic simulation of elastocapillarity. *Meccanica* 53, 6 (2018), 1221–1237.
- Oleksiy Busaryev, Tamal K Dey, Huamin Wang, and Zhong Ren. 2012. Animating bubble interactions in a liquid foam. *ACM Transactions on Graphics (TOG)* 31, 4 (2012), 1–8.
- Hans-Jürgen Butt and Michael Kappl. 2018. *Surface and interfacial forces*. John Wiley & Sons.
- Zhen Cao, Mark J Stevens, and Andrey V Dobrynin. 2014. Elastocapillarity: adhesion and wetting in soft polymeric systems. *Macromolecules* 47, 18 (2014), 6515–6521.
- Zhizhu Cao, Dongliang Sun, Jinjia Wei, Bo Yu, and Jingfa Li. 2019. A coupled volume-of-fluid and level set method based on general curvilinear grids with accurate surface tension calculation. *J. Comput. Phys.* 396 (2019), 799–818.
- Mark Carlson, Peter J Mucha, and Greg Turk. 2004. Rigid fluid: animating the interplay between rigid bodies and fluid. *ACM Transactions on Graphics (TOG)* 23, 3 (2004), 377–384.
- Jingyu Chen, Victoria Kala, Alan Marquez-Razon, Elias Gueidon, David AB Hyde, and Joseph Teran. 2021. A momentum-conserving implicit material point method for surface tension with contact angles and spatial gradients. *ACM Transactions on Graphics (TOG)* 40, 4 (2021), 1–16.
- Adam E Cohen and L Mahadevan. 2003. Kinks, rings, and rackets in filamentous structures. *Proceedings of the National Academy of Sciences* 100, 21 (2003), 12141–12146.
- Pierre Colinet, Jean Claude Legros, and Manuel G Velarde. 2001. *Nonlinear dynamics of surface-tension-driven instabilities*. Vol. 527. Wiley Online Library.
- Nathan B Crane, Onursal Onen, Jose Carballo, Qi Ni, and Rasim Guldiken. 2013. Fluidic assembly at the microscale: progress and prospects. *Microfluidics and nanofluidics* 14, 3 (2013), 383–419.
- Fang Da, Christopher Batty, Chris Wojtan, and Eitan Grinspun. 2015. Double bubbles sans toil and trouble: Discrete circulation-preserving vortex sheets for soap films and foams. *ACM Transactions on Graphics* 34, 4 (2015), 1–9.
- Fang Da, David Hahn, Christopher Batty, Chris Wojtan, and Eitan Grinspun. 2016a. Surface-only liquids. *ACM Transactions on Graphics* 35, 4 (2016), 1–12.
- Fang Da, David Hahn, Christopher Batty, Chris Wojtan, and Eitan Grinspun. 2016b. Surface-only liquids. *ACM Transactions on Graphics (TOG)* 35, 4 (2016), 1–12.
- Sanjeev P Dalawai, Mohamed Aly Saad Aly, Sanjay S Latthe, Ruimin Xing, Rajaram S Sutar, Saravanan Nagappan, Chang-Sik Ha, Kishor Kumar Sadasivuni, and Shanhu Liu. 2020. Recent advances in durability of superhydrophobic self-cleaning technology: a critical review. *Progress in Organic Coatings* 138 (2020), 105381.
- Nikola A Dudukovic, Erika J Fong, Hawi B Gameda, Joshua R DeOtte, Maira R Cerón, Bryan D Moran, Jonathan T Davis, Sarah E Baker, and Eric B Duoss. 2021. Cellular fluidics. *Nature* 595, 7865 (2021), 58–65.
- Camille Duprat, Jeffrey M Aristoff, and Howard A Stone. 2011. Dynamics of elastocapillary rise. *Journal of fluid mechanics* 679 (2011), 641–654.
- Camille Duprat and Howard A Shore. 2015. *Fluid-structure interactions in low-Reynolds-number flows*. Royal Society of Chemistry.
- Jens Eggers and Howard A Stone. 2004. Characteristic lengths at moving contact lines for a perfectly wetting fluid: the influence of speed on the dynamic contact angle. *Journal of Fluid Mechanics* 505 (2004), 309–321.
- Lawrence C Evans. 2010. *Partial differential equations*. Vol. 19. American Mathematical Soc.
- Robert Evans, Maria C Stewart, and Nigel B Wilding. 2019. A unified description of hydrophilic and superhydrophobic surfaces in terms of the wetting and drying transitions of liquids. *Proceedings of the National Academy of Sciences* 116, 48 (2019), 23901–23908.
- Samuel Fagbemi, Pejman Tahmasebi, and Mohammad Piri. 2020. Elastocapillarity modeling of multiphase flow-induced solid deformation using volume of fluid method. *J. Comput. Phys.* 421 (2020), 109641.
- JingCun Fan, Joël De Coninck, HengAn Wu, and FengChao Wang. 2020. Microscopic origin of capillary force balance at contact line. *Physical Review Letters* 124, 12 (2020), 125502.
- Ronald Fedkiw, Jos Stam, and Henrik Wann Jensen. 2001. Visual simulation of smoke. In *Proceedings of the 28th annual conference on Computer graphics and interactive techniques*. 15–22.
- Yun Fei, Christopher Batty, Eitan Grinspun, and Changxi Zheng. 2018. A multi-scale model for simulating liquid-fabric interactions. *ACM Transactions on Graphics (TOG)* 37, 4 (2018), 1–16.
- Yun Fei, Henrique Teles Maia, Christopher Batty, Changxi Zheng, and Eitan Grinspun. 2017. A multi-scale model for simulating liquid-hair interactions. *ACM Transactions on Graphics (TOG)* 36, 4 (2017), 1–17.
- Morris R Flynn and John WM Bush. 2008. Underwater breathing: the mechanics of plastron respiration. *Journal of Fluid Mechanics* 608 (2008), 275–296.
- Nick Foster and Ronald Fedkiw. 2001. Practical animation of liquids. In *Proceedings of the 28th annual conference on Computer graphics and interactive techniques*. 23–30.
- Sean Gart, Joseph E Mates, Constantine M Megaridis, and Sunghwan Jung. 2015. Droplet impacting a cantilever: A leaf-raindrop system. *Physical Review Applied* 3, 4 (2015), 044019.
- Olivier Gènevaux, Arash Habibi, and Jean-Michel Dischler. 2003. Simulating Fluid-Solid Interaction. In *Graphics interface*, Vol. 2003. Citeseer, 31–38.
- Eran Guendelman, Andrew Selle, Frank Losasso, and Ronald Fedkiw. 2005. Coupling water and smoke to thin deformable and rigid shells. *ACM Transactions on Graphics* 24, 3 (2005), 973–981.
- Guang-Ping Hao, Giovanni Mondin, Zhikun Zheng, Tim Biemelt, Stefan Klosz, René Schubel, Alexander Eychmüller, and Stefan Kaskel. 2015. Unusual Ultra-Hydrophilic, Porous Carbon Cuboids for Atmospheric-Water Capture. *Angewandte Chemie International Edition* 54, 6 (2015), 1941–1945.
- Matthias Heil and Joseph P White. 2002. Airway closure: surface-tension-driven non-axisymmetric instabilities of liquid-lined elastic rings. *Journal of Fluid Mechanics* 462 (2002), 79–109.
- Yuanming Hu, Yu Fang, Ziheng Ge, Ziyin Qu, Yixin Zhu, Andre Pradhana, and Chenfanfu Jiang. 2018. A moving least squares material point method with displacement discontinuity and two-way rigid body coupling. *ACM Transactions on Graphics (TOG)* 37, 4 (2018), 1–14.
- Jiangshui Huang, Megan Juszkiewicz, Wim H De Jeu, Enrique Cerda, Todd Emrick, Narayanan Menon, and Thomas P Russell. 2007. Capillary wrinkling of floating thin polymer films. *Science* 317, 5838 (2007), 650–653.
- Weizhen Huang, Julian Iseringhausen, Tom Kneiphof, Ziyin Qu, Chenfanfu Jiang, and Matthias B Hulin. 2020. Chemomechanical simulation of soap film flow on spherical bubbles. *ACM Transactions on Graphics (TOG)* 39, 4 (2020), 41–1.
- Markus Huber, Simon Pabst, and Wolfgang Straßer. 2011. Wet cloth simulation. In *ACM SIGGRAPH 2011 Posters*. 1–1.
- David AB Hyde, Steven W Gagniere, Alan Marquez-Razon, and Joseph Teran. 2020. An implicit updated lagrangian formulation for liquids with large surface energy. *ACM Transactions on Graphics (TOG)* 39, 6 (2020), 1–13.
- Sadashige Ishida, Masafumi Yamamoto, Ryoichi Ando, and Toshiya Hachisuka. 2017. A hyperbolic geometric flow for evolving films and foams. *ACM Transactions on Graphics (TOG)* 36, 6 (2017), 1–11.

- Gillian B Kaggwa, Prathima C Nalam, Jason I Kilpatrick, Nicholas D Spencer, and Suzanne P Jarvis. 2012. Impact of hydrophilic/hydrophobic surface chemistry on hydration forces in the absence of confinement. *Langmuir* 28, 16 (2012), 6589–6594.
- Stefan Karpitschka, S Das, Mathijs van Gorcum, Hugo Perrin, Bruno Andreotti, and Jacco H Snoeijer. 2015. Droplets move over viscoelastic substrates by surfing a ridge. *Nature communications* 6, 1 (2015), 1–7.
- Ron Kimmel and James A Sethian. 1998. Computing geodesic paths on manifolds. *Proceedings of the national academy of Sciences* 95, 15 (1998), 8431–8435.
- Bryan M Klingner, Bryan E Feldman, Nuttapong Chentanez, and James F O'brien. 2006. Fluid animation with dynamic meshes. In *ACM SIGGRAPH 2006 Papers*. 820–825.
- Gregory Lecrivain, Taisa Beatriz Pacheco Grein, Ryoichi Yamamoto, Uwe Hampel, and Takashi Taniguchi. 2020. Eulerian/Lagrangian formulation for the elasto-capillary deformation of a flexible fibre. *J. Comput. Phys.* 409 (2020), 109324.
- Minjae Lee, David Hyde, Michael Bao, and Ronald Fedkiw. 2018. A skinned tetrahedral mesh for hair animation and hair-water interaction. *IEEE transactions on visualization and computer graphics* 25, 3 (2018), 1449–1459.
- Minjae Lee, David Hyde, Kevin Li, and Ronald Fedkiw. 2019. A robust volume conserving method for character-water interaction. In *Proceedings of the 18th annual ACM SIGGRAPH/Eurographics Symposium on Computer Animation*. 1–12.
- Antoine Legrain, Erwin JW Berenschot, Leon Abelmann, José Bico, and Niels R Tas. 2016. Let's twist again: elasto-capillary assembly of parallel ribbons. *Soft matter* 12, 34 (2016), 7186–7194.
- Timothy G Leong, Aasiyeh M Zarafshar, and David H Gracias. 2010. Three-dimensional fabrication at small size scales. *small* 6, 7 (2010), 792–806.
- Claire Lestringant and Basile Audoly. 2020. A one-dimensional model for elasto-capillary necking. *Proceedings of the Royal Society A* 476, 2240 (2020), 20200337.
- Chong Li, Jian Zhang, Jun Han, and Banghua Yao. 2021. A numerical solution to the effects of surface roughness on water-coal contact angle. *Scientific Reports* 11, 1 (2021), 1–12.
- Heyi Liang, Zhen Cao, Zilu Wang, and Andrey V Dobrynin. 2018. Surface stresses and a force balance at a contact line. *Langmuir* 34, 25 (2018), 7497–7502.
- Laurent Limat. 2012. Straight contact lines on a soft, incompressible solid. *The European Physical Journal E* 35, 12 (2012), 1–13.
- Jian-Lin Liu and Xi-Qiao Feng. 2012. On elastocapillarity: A review. *Acta Mechanica Sinica* 28, 4 (2012), 928–940.
- Kesong Liu and Lei Jiang. 2012. Bio-inspired self-cleaning surfaces. *Annual Review of Materials Research* 42 (2012), 231–263.
- Qihan Liu, Tetsu Uuchi, Lihua Jin, Ryan Hayward, and Zhigang Suo. 2019. Elastocapillary crease. *Physical review letters* 122, 9 (2019), 098003.
- William E Lorensen and Harvey E Cline. 1987. Marching cubes: A high resolution 3D surface construction algorithm. *ACM siggraph computer graphics* 21, 4 (1987), 163–169.
- CH Mastrangelo and CH Hsu. 1993. Mechanical stability and adhesion of microstructures under capillary forces. II. Experiments. *Journal of Microelectromechanical systems* 2, 1 (1993), 44–55.
- Joseph P Morris. 2000. Simulating surface tension with smoothed particle hydrodynamics. *International journal for numerical methods in fluids* 33, 3 (2000), 333–353.
- C Neinhuis and W Barthlott. 1997. Characterization and distribution of water-repellent, self-cleaning plant surfaces. *Annals of botany* 79, 6 (1997), 667–677.
- Shunsuke Nishimoto and Bharat Bhushan. 2013. Bioinspired self-cleaning surfaces with superhydrophobicity, superoleophobicity, and superhydrophilicity. *Rsc Advances* 3, 3 (2013), 671–690.
- Stéphane Popinet. 2018. Numerical models of surface tension. *Annual Review of Fluid Mechanics* 50 (2018), 49–75.
- Lawrence R Pratt and David Chandler. 1977. Theory of the hydrophobic effect. *The Journal of chemical physics* 67, 8 (1977), 3683–3704.
- Charlotte Py, Paul Reverdy, Lionel Doppler, José Bico, Benoit Roman, and Charles N Baroud. 2007. Capillary origami: spontaneous wrapping of a droplet with an elastic sheet. *Physical review letters* 98, 15 (2007), 156103.
- Avi Robinson-Mosher, Tamar Shinar, Jon Gretarsson, Jonathan Su, and Ronald Fedkiw. 2008. Two-way coupling of fluids to rigid and deformable solids and shells. *ACM Transactions on Graphics* 27, 3 (2008), 1–9.
- Benoit Roman and José Bico. 2010. Elasto-capillarity: deforming an elastic structure with a liquid droplet. *Journal of Physics: Condensed Matter* 22, 49 (2010), 493101.
- Liangwang Ruan, Jinyuan Liu, Bo Zhu, Shinjiro Sueda, Bin Wang, and Baoquan Chen. 2021. Solid-fluid interaction with surface-tension-dominant contact. *ACM Transactions on Graphics (TOG)* 40, 4 (2021), 1–12.
- Witawat Rungjiratananon, Yoshihiro Kanamori, and Tomoyuki Nishita. 2012. Wetting effects in hair simulation. In *Computer Graphics Forum*, Vol. 31. Wiley Online Library, 1993–2002.
- Craig Schroeder, Wen Zheng, and Ronald Fedkiw. 2012. Semi-implicit surface tension formulation with a Lagrangian surface mesh on an Eulerian simulation grid. *J. Comput. Phys.* 231, 4 (2012), 2092–2115.
- Sushanta Kumar Sethi and Gaurav Manik. 2018. Recent progress in super hydrophobic/hydrophilic self-cleaning surfaces for various industrial applications: a review. *Polymer-Plastics Technology and Engineering* 57, 18 (2018), 1932–1952.
- James A Sethian and Peter Smereka. 2003. Level set methods for fluid interfaces. *Annual review of fluid mechanics* 35, 1 (2003), 341–372.
- Eftychios Sifakis and Jernej Barbic. 2012. FEM simulation of 3D deformable solids: a practitioner's guide to theory, discretization and model reduction. In *Acn siggraph 2012 courses*. 1–50.
- Kiran Singh, John R Lister, and Dominic Vella. 2014. A fluid-mechanical model of elastocapillary coalescence. *Journal of fluid mechanics* 745 (2014), 621–646.
- Alexandre Tartakovsky and Paul Meakin. 2005. Modeling of surface tension and contact angles with smoothed particle hydrodynamics. *Physical Review E* 72, 2 (2005), 026301.
- Nils Thürey, Chris Wojtan, Markus Gross, and Greg Turk. 2010. A multiscale approach to mesh-based surface tension flows. *ACM Transactions on Graphics (TOG)* 29, 4 (2010), 1–10.
- EH Van Brummelen, M Shokrpour-Roudbari, and GJ Van Zwieten. 2016. Elasto-capillarity simulations based on the Navier–Stokes–Cahn–Hilliard equations. In *Advances in Computational Fluid-Structure Interaction and Flow Simulation*. Springer, 451–462.
- W Merlijn Van Spengen, Robert Puers, and Ingrid De Wolf. 2002. A physical model to predict stiction in MEMS. *Journal of micromechanics and microengineering* 12, 5 (2002), 702.
- Nicolas Vandewalle, Martin Poty, Nathan Vanesse, Jérémie Caprasse, Thomas Defize, and Christine Jérôme. 2020. Switchable self-assembled capillary structures. *Soft Matter* 16, 45 (2020), 10320–10325.
- Hui Wang, Yongxu Jin, Anqi Luo, Xubo Yang, and Bo Zhu. 2020. Codimensional surface tension flow using moving-least-squares particles. *ACM Transactions on Graphics (TOG)* 39, 4 (2020), 42–1.
- Huamin Wang, Gavin Miller, and Greg Turk. 2007. Solving general shallow wave equations on surfaces. In *Proceedings of the 2007 ACM SIGGRAPH/Eurographics symposium on Computer animation*. 229–238.
- Huamin Wang, Peter J Mucha, and Greg Turk. 2005. Water drops on surfaces. *ACM Transactions on Graphics* 24, 3 (2005), 921–929.
- Mengdi Wang, Yitong Deng, Xiangxin Kong, Aditya H Prasad, Shiyong Xiong, and Bo Zhu. 2021. Thin-film smoothed particle hydrodynamics fluid. *ACM Transactions on Graphics (TOG)* 40, 4 (2021), 1–16.
- Zhiyan Wei, Tobias M Schneider, Jungchul Kim, H-Y Kim, Joanna Aizenberg, and Lakshminarayanan Mahadevan. 2015. Elastocapillary coalescence of plates and pillars. *Proceedings of the Royal Society A: Mathematical, Physical and Engineering Sciences* 471, 2175 (2015), 20140593.
- Tao Yang, Ralph R Martin, Ming C Lin, Jian Chang, and Shi-Min Hu. 2017. Pairwise force SPH model for real-time multi-interaction applications. *IEEE transactions on visualization and computer graphics* 23, 10 (2017), 2235–2247.
- Yuehua Yuan and T Randall Lee. 2013. Contact angle and wetting properties. In *Surface science techniques*. Springer, 3–34.
- Junping Zhang and Stefan Seeger. 2011. Polyester materials with superwetting silicone nanofilaments for oil/water separation and selective oil absorption. *Advanced Functional Materials* 21, 24 (2011), 4699–4704.
- Wen Zheng, Jun-Hai Yong, and Jean-Claude Paul. 2009. Simulation of bubbles. *Graphical Models* 71, 6 (2009), 229–239.
- Wen Zheng, Bo Zhu, Byungmoon Kim, and Ronald Fedkiw. 2015. A new incompressibility discretization for a hybrid particle MAC grid representation with surface tension. *J. of Computational Physics* 280 (2015), 96–142.
- Bo Zhu, Minjae Lee, Ed Quigley, and Ronald Fedkiw. 2015. Codimensional non-Newtonian fluids. *ACM Transactions on Graphics* 34, 4 (2015), 1–9.
- Bo Zhu, Ed Quigley, Matthew Cong, Justin Solomon, and Ronald Fedkiw. 2014. Codimensional surface tension flow on simplicial complexes. *ACM Transactions on Graphics (TOG)* 33, 4 (2014), 1–11.